Efficient radioactive gas detection by scintillating porous metal–organic frameworks

M. Orfano, J. Perego, F. Cova, C.X. Bezuidenhout, S. Piva, Christophe Dujardin, Benoit Sabot, Sylvie Pierre, Pavlo Mai, C. Daniel, et al.

Efficient radioactive gas detection

by porous metal-organic framework scintillating nanocrystals.

M. Orfano[1↓], J. Perego[1↓], F. Cova[1], C. X. Bezuidenhout[1], S. Piva[1], C. Dujardin[2], B. Sabot[3], S. Pierre[3], P. Mai[2], C. Daniel[4], S. Bracco[1], A. Vedda[1*], A. Comotti[1,*], A. Monguzzi[1,*]

[1] *Dipartimento di Scienza dei Materiali, Università degli Studi Milano-Bicocca, Milano – ITALY*

[2] *Institut Lumière Matière, Université Claude Bernard Lyon 1, Lyon – France*

[3] *Université Paris-Saclay, CEA, LIST, Laboratoire National Henri Becquerel (LNE-LNHB), F-91120 Palaiseau – France*

[4] *Nano Active Film SRL, Dipartimento di Chimica e Biologia, Università degli Studi di Salerno, Fisciano (SA) - Italy*

E-mail: anna.vedda@unimib.it - angiolina.comotti@unimib.it - angelo.monguzzi@unimib.it

[↓]: these authors contributed equally.

ABSTRACT

Natural radioactive gases and anthropogenic radionuclides such as radon, xenon, hydrogen and krypton isotopes, need to be carefully monitored to be properly managed as pathogenic agents, radioactive diagnostic agents or indicators of nuclear activity. State-of-the-art gas detectors based on liquid scintillators suffer from many drawbacks such as lengthy sample preparation procedures and limited solubility of gaseous radionuclides, which produces a detrimental effect on measurement sensitivity. A potential breakthrough solution to this problem is using solid porous scintillators that act as gas concentrators and, therefore, could increase detection sensitivity. Highly porous scintillating metal-organic frameworks (MOFs) stand out as relevant materials for the realization of these devices. We demonstrate the capability of porous hafnium-based MOF nanocrystals exploiting dicarboxy-9,10-diphenylanthracene (DPA) as a scintillating conjugated ligand to detect gas radionuclides. The nanocrystals show fast scintillation properties in the nanosecond domain, a fluorescence quantum yield of ~40% and an accessible porosity suitable to host noble gas atoms and ions. The adsorption and detection of radionuclides such as ^{85}Kr, ^{222}Rn and ^{3}H have been explored for these MOFs utilising a newly developed device based on a time coincidence technique. MOF nanocrystals demonstrate an improved sensitivity for these radionuclides compared to a reference detector, showing an excellent linear response down to an activity value lower than 1 $kBq \cdot m^{-3}$ that outperforms commercial devices. These results strongly support the possible use of scintillating porous MOF nanocrystals as the building block of ultrasensitive sensors for detecting natural and anthropogenic radioactive gases.

INTRODUCTION

Natural radioactive gases, such as the isotopes of radon (^{222}Rn and ^{220}Rn) and the anthropogenic radionuclides coming from fission products (Xe and ^{85}Kr isotopes) and activation products (^{3}H and ^{37}Ar), need to be carefully monitored. For example, isotopes such as ^{85}Kr and ^{3}H, which originate from nuclear power plants, reprocessing plants and nuclear waste treatments,[1-5] are critical to detect for monitoring nuclear activity and providing feedback to the national or international authorities to evaluate the nuclear environmental impact. Precise detection of ^{85}Kr variation concentration in air can also play a crucial role in detecting illegal reprocessing of nuclear fuel to produce plutonium for weapons.[6] Finally, Xe isotopes and ^{37}Ar are of key interest as they can be used to detect clandestine nuclear activities to verify compliance with the Comprehensive Nuclear-Test-Ban Treaty.[13] On the other hand, gas from granite-rich areas (^{222}Rn and ^{220}Rn)[7-9] are pathogenic agents which must be quantified in order to mitigate the exposure risk, while the Xe isotopes can also play a beneficial role as radioactive diagnostic contrast agents for inhalation studies to evaluate pulmonary function, lung imaging and for the assessment of cerebral blood flow.[10-12] Therefore, the detection and radioactivity metrology of gases is a crucial aspect in a modern, technologically advanced and sustainable society, as demonstrated by the recurrent updates of the regulations on this subject, which require the use of increasingly more sensitive and accurate detectors.[14]

All the listed radionuclides, of which radon also produces α particles, decay by emitting pure β particles, i.e. electrons that are challenging to detect due to their short-range path in matter, especially for ^{3}H and, to a lesser degree, ^{85}Kr.[15] The liquid scintillation counting technique is the current gold standard to measure radioactive gases in certified control laboratories. The test is performed by bubbling these gases in water and then sampling this water mixed with an aromatic solvent containing a scintillating fluorophore and surfactant. The detection is then achieved by post sampling using calibrated liquid scintillation counters. Fast scintillators allow using two photomultiplier tubes working in time coincidence, thus reducing the measurement noise and improving both the result accuracy and the detector sensitivity.[16] Unfortunately, this technology has several critical issues. Among them, the intrinsic gas solubility limits the effective amount of gas that can be injected into the scintillating solution to be analysed, thus restricting the instrument sensitivity. Even if this technology gives the opportunity to detect gas with acceptable sensitivity, it requires a laborious sampling and preparation procedure before any measurement: an online gas measurement system with similar or better sensitivity would be a convenient solution. A potential breakthrough development of the technology for radioactive gas detection is to realize a solid porous scintillator: the adsorption of gases in the porous framework would concentrate the radionuclides to a higher level than in liquid, simultaneously enhancing the probability of interaction of the scintillating material with the emitted ionizing radiation generated in the inner part of the detector, thus increasing the device sensitivity. In addition, the porous architecture enables the direct bypass of the critical practical issue of bubbling radioactive gases into liquids and sampling, plus post-sampling measurement in a dedicated laboratory. At the same time, it avoids radioactive-liquid-organic waste and its demanding management and disposal. Therefore, porous scintillators are proposed as a new class of scintillating materials for the development of highly responsive radioactive gas detectors based on time-coincidence techniques,[17] as sketched in Figure 1A.

Metal-organic frameworks (MOFs) endowed with high porosity and scintillating properties are excellent candidates for realising efficient radioactive gas detectors. The controlled self-assembly of inorganic nodes and organic ligands produces tailored framework architectures with a specific topology and well-defined porosity for gas capture, selective adsorption and separation, and storage.[18-20] Moreover, highly luminescent conjugated chromophores, included as ligands or luminescent guests, produce emissive materials with unique photophysical [21-24] and scintillating properties.[22-24] Nevertheless, despite the increasing number of reports about the development of MOFs as effective scintillators, to date, their potential application as scintillating materials for the detection of radioactive gases has not yet been reported. The only examples in literature describe the general luminescence properties of MOFs being sensitive to the presence of specific radioactive heavy-metal ions,[25] or to the use of MOFs as sorbents for the removal of radionuclides.[26, 27]

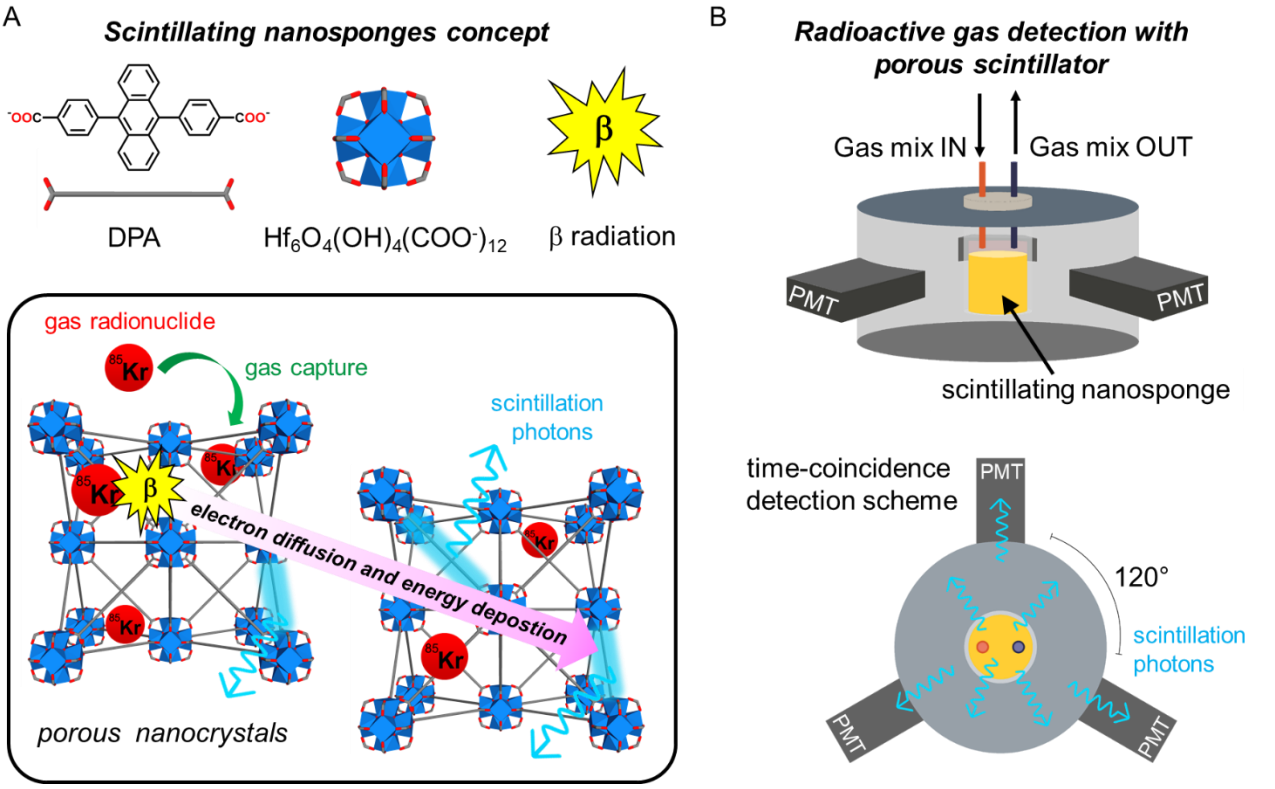

Figure 1 | Time-coincidence based detector for radionuclides gases exploiting porous nanoscintillators. (A) Schematic representation of the scintillation mechanism inside fluorescent hafnium-based MOF nanocrystals. The porous frameworks can uptake radioactive gaseous species through physical adsorption and concentrate them inside the pores. The decay process produces β particles that can effectively interact with the nanocrystals during their diffusion and thermalization, triggering a sensitized scintillation process. (B) Sketch of the triple-coincidence system designed to reveal radioactive gases by exploiting a porous scintillator. The porous material is placed in the central chamber where it adsorbs the flowing gas molecules, whose β decay produces high-energy electrons in the pores. The interactions of electrons with the walls of the pores generate the light pulses to be recorded by three symmetric photomultiplier tubes (PMTs) employed to have a low-noise time-coincidence detection.

Here we demonstrate the capability of porous hafnium-based MOF nanocrystals exploiting dicarboxy-9,10-diphenylanthracene (DPA) as a scintillating organic ligand (Figure 1B) for gas radioactivity detection. The nanocrystals show a highly accessible porosity suitable to host noble gas atoms and ions, fast scintillation properties in the nanosecond time range appropriate for time-coincidence-based detection techniques and a good fluorescence quantum yield of ~40%. The presence of a heavy element such as hafnium enables a good light intensity output under excitation ionizing radiation, i.e. one order of magnitude larger than a commercial plastic scintillator. The achieved excellent properties prompt us to test the sorption and detection of ^{85}Kr, ^{222}Rn and ^{3}H radionuclides in a newly developed device that exploits the nanoscintillator crystalline powder as a gas harvester and concentrator (Figure 1A). The porous MOF nanocrystals show an improved sensitivity with respect to the reference scintillating powders currently tested for gas detection, as well as an excellent linear response down to an activity value well below 1 $kBq \cdot m^{-3}$, thus outperforming some of the available commercial detectors for noble gas radionuclides in a more compact and easy-to-handle architecture. Therefore, these results strongly support the possible use of scintillating porous MOF nanocrystals as active components to fabricate technologically superior sensors for detecting natural and anthropogenic radioactive gases at ultralow concentrations.

RESULTS AND DISCUSSION

Synthesis, gas adsorption and photoluminescence properties of hafnium-based MOF nanocrystals. Hf-based MOF nanocrystals comprising luminescent DPA ligands (Hf-DPA) were obtained by solvothermal syntheses modulated by the relative amount of formic acid that regulates their crystal size (Methods and

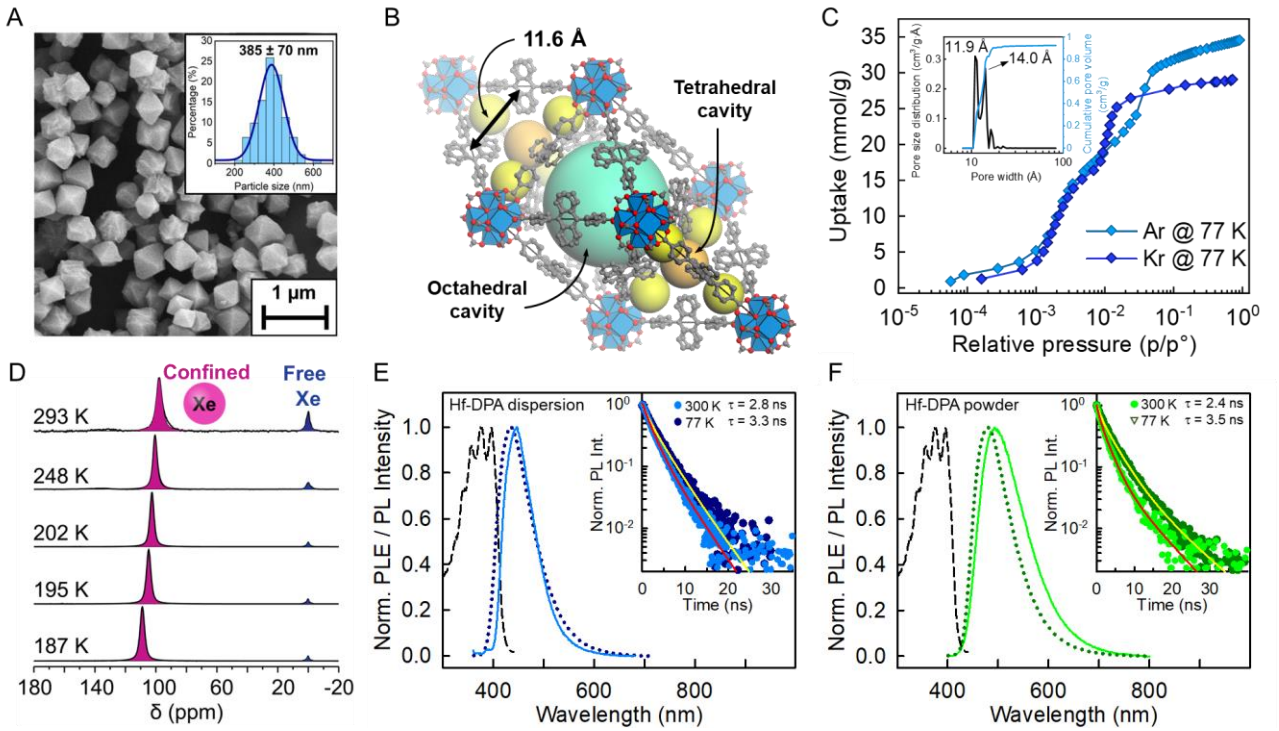

Figure 2 | Structural, gas adsorption, and photoluminescence properties of fluorescent porous Hf-DPA nanocrystals. (A) Scanning electron microscopy (SEM) image of Hf-DPA nanocrystals. The inset depicts the nanocrystal size distribution obtained by SEM image analysis. (B) Crystal structure of Hf-DPA highlighting the octahedral and tetrahedral cavities. Triangular pore window and center-to-center distance between DPA molecules are highlighted. (C) Ar (light blue) and Kr (dark blue) adsorption isotherms collected at 77 K. Inset: pore size distribution calculated from Ar adsorption isotherm using NL-DFT method. (D) Hyperpolarized ^{129}Xe NMR spectra of Hf-DPA at variable temperature. (E) Excitation photoluminescence (PLE, dashed line) and photoluminescence emission (PL) spectra of MOF nanocrystals dispersed in THF (5×10^{-8} M, top panel) or as (F) bare powder (low panel). The PL has been recorded at 300 K (solid line) and 77 K (dotted line). The excitation wavelength is 355 nm. The insets show the PL intensity decay as a function of time recorded at the PL maximum emission wavelength under 340 nm pulsed excitation. The solid lines represent the fit of data with multi-exponential decay functions that results in the average emission lifetime values reported.

Figure S4-S7).[23,24] The synthesis was optimized to produce octahedral nanocrystals with 385 nm diameter (Figure 2A) in highly reproducible batches of ~ 200 mg (Supplementary Figures S8-S11). The structure was solved by Rietveld refinement combined with PW-DFT of synchrotron-source PXRD pattern collected at 298/293 K (Figure S15-S17). The Hf-DPA nanocrystals display a cubic crystal structure (space group F*m-3m*) with **fcu** topology comprising octahedral and tetrahedral cavities (10.2 and 17 Å diameter fitted spheres, respectively). These cavities are connected by triangular windows through which a sphere of 5.3 Å in diameter can pass, thus yielding highly connected three-dimensional pores enclosed in the framework (Figure 2B and Figure S18-S20). The total available pore volume corresponds to 70%, as explored by a sphere of 1.82 Å radius. FT-IR, ^{13}C MAS NMR spectroscopy and TGA demonstrated the purity and thermal stability of the compounds (Figure S21-S27). Gas adsorption isotherms demonstrate the microporous nature of Hf-DPA nanocrystals. The N_2 adsorption isotherm collected at 77 K (Figure S28) shows an uptake as high as 29.7 mmol g^{-1} and surface areas of 2887 m^2 g^{-1} and 2613 m^2 g^{-1} according to Langmuir and BET models, respectively. Notably, as depicted in Figure 2C, also noble gases such as Ar and Kr are effectively adsorbed (Figure S29). At low partial pressure and 77 K, the adsorption isotherms display sequential gas adsorption at distinct pressures consistent with the filling of the smaller tetrahedral cavity, followed by the larger octahedral one with mean pore sizes of 10.9 Å and 14.0 Å, respectively, consistent with the crystal structure. Importantly, a complete pore filling is already achieved at a partial pressure as low as 0.2 p/p°, indicating the full accessibility of both pores for all the tested gases. A distinct behavior is observed for the exploration of the octahedral cavity by Ar with respect to the larger Kr. The latter fills these pores at a lower pressure than Ar, owing to stronger Kr-Kr interactions. The pore volume estimated by Ar (R_{vdW} = 1.8 Å) and N_2 (R_{vdW} = 1.82 Å) is 0.92 $cm^3 \cdot g^{-1}$, which agrees with the pore volume calculated from the crystal structure (Supplementary Table S3).

The Ar and Kr adsorption isotherms were also measured at room temperature, demonstrating the gas diffusion inside the cavities under pressure and temperature conditions comparable to the operational scenario of radioactive-gas detection (Figures S30). In this regard, we provide a direct detection of noble gas diffusion into the pores of the Hf-MOF by hyperpolarized ^{129}Xe NMR experiments (Methods). This laser-assisted technique is based on the excitation transfer from the optically pumped rubidium vapors to the ^{129}Xe atoms, increasing the polarization by hundreds of times with respect to the NMR signal of Xe nuclei under thermal equilibrium conditions. Thus, signals can be recorded with high sensitivity even at low Xe concentrations.[24,28-31] Importantly, the hyperpolarized ^{129}Xe gas is diluted at 2% in a mixture of N_2 (4%) and He (94%), demonstrating the effective uptake of Xe even in competition with other gaseous species and under flow conditions. The ^{129}Xe mixture flows into the main magnetic field and immediately diffuses in the MOF pores, reporting information on the preferred adsorption sites of the open framework. The remarkable downfield signal, compared to that of the free gas, is diagnostic of the restricted space explored by the noble gas. It is worth noting that the noble gas Xe possesses a van der Waals radius of 2.16 Å which is intermediate and comparable to those of Kr and Rn (2.02 Å and 2.2 Å, respectively), thus hyperpolarized ^{129}Xe NMR is a suitable technique to demonstrate the accessibility of radionuclides of interest in the Hf-MOF pores of under low pressure and flow conditions. As shown in Figure 2D, at room temperature, an isotropic signal was detected at δ = 97.7 ppm within 200 ms from Xe delivery to Hf-DPA, proving the fast diffusion of Xe atoms through the pores into the confining cavities. This result directly unveils the ability of Hf-DPA to adsorb noble gases, supporting their use as porous nanoscintillators for the capture and detection of radioactive gaseous krypton, radon and xenon isotopes. On lowering temperature, the resonances move to even higher chemical shifts due to the longer residence time close to the pore walls.[32]

Figure 2E shows the steady state photoluminescence and excitation photoluminescence (PLE) spectra of Hf-DPA nanocrystals dispersed in tetrahydrofuran (THF, refractive index n = 1.40 at 480 nm, 10^{-10} M, Methods). Under UV excitation, the dispersion exhibits a blue fluorescence with a maximum at 450 nm and a characteristic average decay time of 2.8 ns, with a good photoluminescence quantum yield, defined as the ratio between the number of emitted photons with respect to those absorbed, of 0.41 ± 0.06 (Methods and Supplementary Information). The PLE profile recorded at the emission maximum matches the vibronic structure of isolated DPA molecules, thus indicating the absence of large amounts of aggregated undesired species that can affect the nanocrystal luminescence properties.[33] Low-temperature measurements show a slight blue shift of the photoluminescence maximum to 440 nm, ascribed to the band narrowing at cryogenic temperatures, which reduces self-absorption and increments the photoluminescence lifetime up to 3.3 ns, which marks an increase of the emission yield up to $0.41 \times \frac{3.3\ ns}{2.8\ ns} = 0.48$ (+18%). This result confirms the absence of significant thermal quenching of photoluminescence in Hf-DPA nanocrystals by intramolecular vibrational mechanisms on ligands, as previously observed for similar systems.[23,24,33] Figure 2F reports the photoluminescence properties of the bare Hf-DPA nanocrystals in powder form that is used to detect the gaseous radionuclides. The emission peak at room temperature is red shifted to 490 nm because of the inner filter effect of self-absorption in the powder form, while the PLE profile is comparable to that of the THF dispersion. The emission lifetime of 2.4 ns is basically unchanged with respect to that in dispersion, thus demonstrating that the nanocrystals maintain their fast emission properties, which are exploited for radioactive gas detection. At 77 K, the emission maximum is again slightly blue shifted to 480 nm with an increment up to 3.5 ns of the lifetime, confirming that the excited state electronic properties of the MOF powder are fully consistent with those of single crystals in diluted dispersion.

Scintillation properties of Hf-DPA nanocrystals.

The scintillation properties of MOF nanocrystals are investigated under soft X-ray excitation. Figure 3A shows the steady-state scintillation (radioluminescence) emission spectrum of Hf-DPA nanocrystals compared to the commercial plastic scintillator EJ-276® as grinded powder (Methods). The nanocrystal radioluminescence matches the respective photoluminescence profile (Figure 2F), suggesting that photons are produced by radiative recombination of molecular excitons produced on the MOF fluorescent ligands through the recombination of free charges generated by the X-rays interaction with matter. Despite the Hf-DPA crystal density of 0.6 - 0.7 g cm^{-3} being significantly lower than the 1.1 g·cm^{-3} of the EJ-276®, the

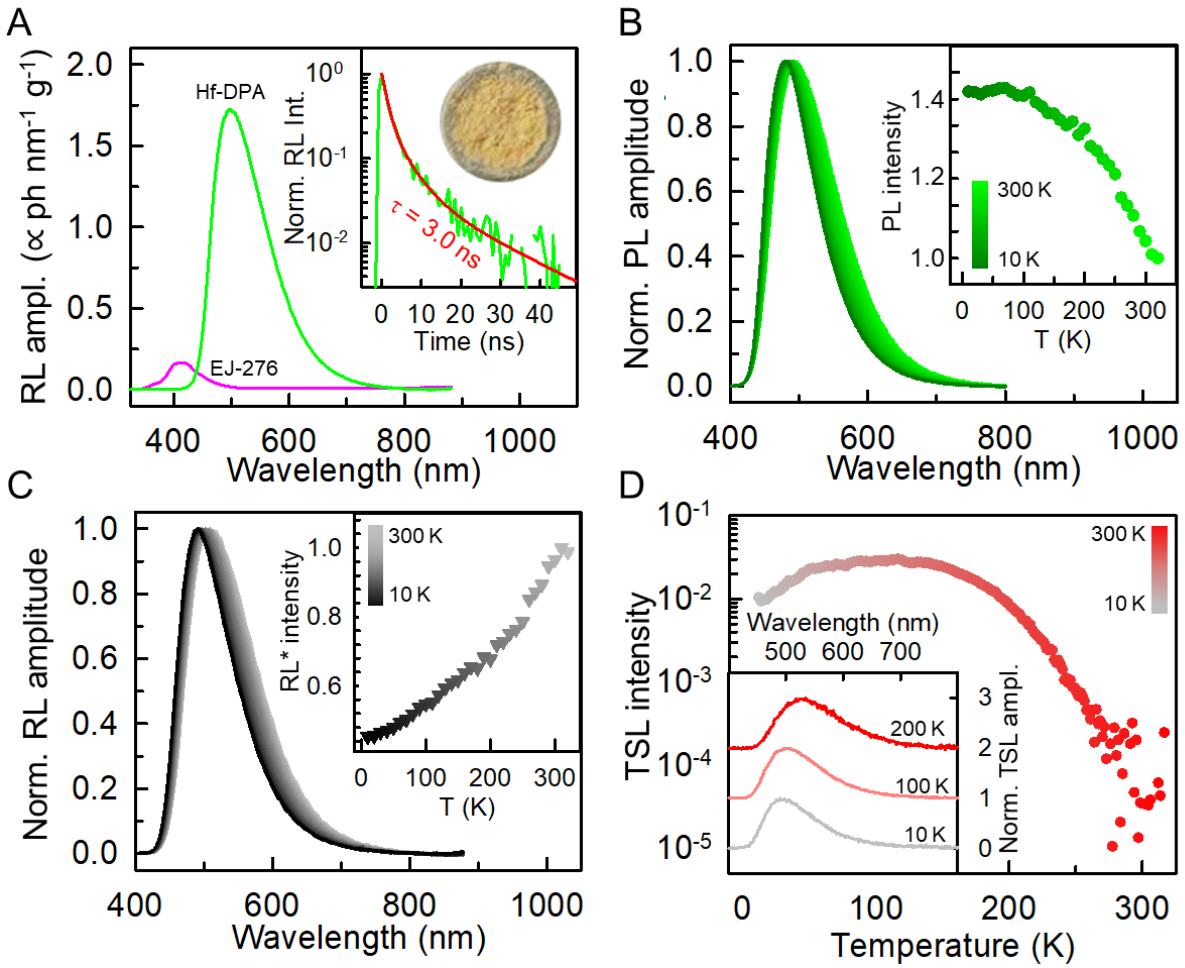

Figure 3 | Scintillation properties of Hf-DPA MOF nanocrystals powder. (A) Radioluminescence (RL) spectrum of Hf-MOFs and plastic EJ-276® scintillator powders under soft X-rays. The inset shows the scintillation pulse recorded for Hf-DPAs with a picture of the MOF powder. The solid line represents the fit with a multi-exponential decay function. (B) Normalized photoluminescence (PL) and (C) RL spectra of Hf-DPA powders as a function of temperature. The insets depict the RL intensity (RL*) normalized to the PL intensity variation reported in panel B as a function of the temperature. (D) Thermally-stimulated luminescence (TSL) intensity of Hf-DPA nanocrystals powder as a function of the temperature, obtained by integrating wavelength resolved measurements in the whole emission region. The inset depicts representative TSL spectra recorded at 10 K, 100 K and 200 K, respectively.

scintillation light generated by the porous nanocrystals is more than one order of magnitude larger (Figure 3A). This efficient emission is owed to the presence of the heavy hafnium ions (Z=72) in the framework, which enhances the interaction with the ionizing radiation allowing to double the scintillation efficiency of the Hf-DPA with respect to the parent zirconium-based MOF (Figure S31), and to the ability of the MOF architecture to sensitize the fluorescent ligand scintillation as recently demonstrated.[23] In parallel, under pulsed X-ray excitation, the nanocrystals produce a fast scintillation pulse, as shown in the inset of Figure 3A. The emitted scintillation pulse shows a sub-nanosecond rise time and a characteristic average emission decay time of 3 ns that matches the recombination decay dynamics of the photoluminescence at room temperature. This finding confirms the origin of the luminescence and indicates that the Hf-DPA fast emission properties are preserved under ionizing radiation excitation.

To better understand the origin of scintillation in MOF nanocrystals, the steady-state photoluminescence and radioluminescence of Hf-DPA nanocrystals have been monitored in parallel as a function of temperature. Figure 3B shows the MOF normalized photoluminescence spectrum recorded by cooling the powder from 300 K down to 10 K. By lowering the temperature, the emission maximum wavelength is blue-shifted from 490 nm to 480 nm, in agreement with the data in Figure 3B, most probably due to a partial mitigation of self-absorption caused by the band narrowing effect at low temperature (from

0.56 meV to 0.50 meV, Supplementary Table 7). The inset shows the photoluminescence intensity increasing by +40% at temperatures below 100 K, which corresponds to an increment of the photoluminescence quantum yield up to ~0.60. This enhancement is even larger than that expected considering the increment of the photoluminescence lifetime at low temperatures (inset of Figure 3B). These findings suggest that additional temperature-dependent deactivation pathways are involved in the nanocrystal partial emission quenching, such as some ultrafast quenching of diffusing charges or molecular excitons by energetic traps that cannot be observed in the nanosecond time scale.[34]

The presence of trap sites is further supported by the results of variable temperature radioluminescence experiments. Figure 3C shows that the radioluminescence spectrum profile changes in accordance with the photoluminescence behaviour with both the same slight band narrowing and blue shift (Supplementary Table 7). The inset reports the radioluminescence intensity corrected by the photoluminescence curve shown in Figure 3B to decouple the intrinsic luminescence dependence on the emitter temperature from all the other mechanisms involved in the scintillation process. This allows us to monitor the effects of temperature before the generation of molecular excitons on the nanocrystal ligands. Conversely to the photoluminescence, the radioluminescence intensity shows a progressive reduction upon lowering the sample temperature, losing about half of its intensity at 10 K. This behaviour is a fingerprint that indicates the presence of trapping sites. Indeed, the trapping mechanism competes with the recombination of diffusing free charges on emissive ligands. Usually, thermal energy can free the trapped charges to be potentially recovered for light generation. Therefore, at low temperatures, the trapped charges are effectively lost, with a consequent reduction of the emission intensity. In contrast, the trap sites are unstable at high temperatures, and a dynamic equilibrium between the trapping of carriers and their thermal release is established. [35]

The role of traps in the scintillation process is investigated by wavelength-resolved thermally stimulated luminescence (TSL) measurements (Methods). The nanocrystals are exposed to ionizing radiation up to around 10 Gy at 10 K, to fill trap sites and avoid their spontaneous depletion because of thermal energy. [36,37] After irradiation, the temperature of the sample is increased with a linear heating rate while monitoring the luminescence produced. This experiment highlights the contribution of de-trapped charges in the production of scintillation light at room temperature. Figure 3D reports the TSL emission spectra at three temperatures (inset) and the TSL intensity as a function of temperature between 10 K and 320 K. The TSL spectral profile closely resembles the radioluminescence and photoluminescence profiles, featuring the same red shift upon heating (Figure S32). This demonstrates that the charge traps present in the system play a role in the scintillation light production at room temperature. The shape of the TSL signal vs. temperature, the so-called *glow curve* of the material, depends on the nature of the traps that are thermally releasing charge carriers. The TSL intensity values have been corrected for the variation of the radioluminescence emission intensity vs. temperature to decouple the trap contribution to the emission from the other mechanisms involved in scintillation. The glow curve is broad and smooth, without any clear signal peak and reaches its maximum intensity at around 100 K. This featureless shape, without any narrow peak structure that marks a specific energy, suggests the existence of a broad energy distribution of trap states,[38,39] in agreement with the smooth radioluminescence and photoluminescence spectra that mirrors the presence of many different local environments and quenching pathways for the nanocrystal emitting ligands (Figure 2F). Notably, the TSL intensity is only a few percent (2.5%) of the total radioluminescence intensity (Supplementary Information), thus indicating that trapped energy has a minor contribution to the room temperature scintillation and does not seriously affect the material scintillation yield.

Radioactive gas detection with MOFs nanocrystals.

The capability of porous Hf-DPA nanocrystals to adsorb noble gases such as Ar, Kr, Xe and Rn at room temperature, to concentrate their radioactive isotopes for detection, was demonstrated by combined experimental and simulated approaches. Figure 4A shows the adsorption isotherms calculated by Grand Canonical Monte Carlo simulations (see Methods and Supplementary information, section 6). Notably, the calculations successfully reproduce the experimental isotherms measured for Ar and Kr, thus demonstrating the validity of the developed modelling as a reliable predictive tool for gas adsorption and diffusion of noble gases such as Ar, Kr, Xe and Rn (Figure S33-S34). Furthermore, the simulated adsorption shows a clear

correlation between the amount of gas adsorbed and their atomic masses, with a preference for the heavier Rn compared to the other gases at a given pressure. Analysing the gas distribution in the pores at a low pressure of 50 millibars and room temperature shows a notable gas-size dependence. The smaller gases, such as Kr, are more homogenously distributed in all the available space (Figure 4B, left), whilst the larger Rn atom is preferably hosted in the smaller tetrahedral cavities (Figure 4B, right). This peculiar behaviour is determined by the gas-matrix interaction energies (Figure S35-S36), which give insight into the affinity and retention capability of the framework towards the exploring gases (Figure 4C) and, in turn, have relevance for selectivity and detection applications in air. Kr gas diffusion modelled in the presence of air (76% N_2 and 21% O_2, and 3% H_2O) probes the speed of gases propagating within the crystals: the calculated Kr diffusion coefficient of the 10^{-4} cm^2 s^{-1} suggests that Kr atoms pervade the nanocrystals of 385 nm diameter within tens of microseconds (Figure S37-S38). The diffusion of the gas molecules through the entire nanocrystal volume in such a short time demonstrates that noble gas radionuclides can be effectively and rapidly adsorbed into the nanoscintillator pores even under standard working conditions, i.e. mixed in air at room temperature.

The ability of Hf-DPA nanocrystals to detect radioactive gases has been tested using a radioactive krypton isotope (^{85}Kr) in a custom-made prototype device (Figure S39). The main β decay of ^{85}Kr (99.562% emission rate) produces an electron spectrum with a maximum emission energy of 687.1 keV and an average energy of 251.4 keV.[40] The radionuclides can be mixed in air at different concentrations, up to hundreds of MBq m^{-3} if necessary, to tune the activity of the air/radionuclide mixture before injection into the sample chamber filled with the porous scintillator. The scintillation photons are then detected by employing a time coincidence measurement technique based on the simultaneous use of two PMTs (Fig. 1B, Methods).[17] Specifically, the isotope activity has been monitored by recording the logical sum of the double coincidence counting rate of the detectors (Supplementary Material). The coincidence technique can be applied using different coincidence windows where the PMTs are activated in order to be adapted to the decay time of the scintillator to maximize the device's sensitivity.[41,42,43] Here, we tested the system using two coincidence windows of 40 ns (as used in standard liquid scintillation) and 400 ns. The longer time window has been chosen to consider the potential effect of slow scintillation mechanisms. Dedicated software was developed for all the measurements to correct the count rate results from accidental coincidences for background and gas measurements. The results obtained for detecting ^{85}Kr radionuclides using a standard scintillating powder, i.e. polystyrene (PS) microspheres of diameter 175±75 μm, [44] and Hf-DPA nanocrystal powder, are reported in Figure 4D. This data highlights a significant difference and improved behaviour of porous nanocrystals compared to the reference sample in detecting ^{85}Kr. First, Hf-DPA nanocrystals generate a scintillation intensity ca. 4.6 and 3.9 times larger than microspheres for 40 ns and 400 ns coincidence windows, respectively. This demonstrates the efficiency of fluorescent MOF nanocrystals as scintillators, hinted by radioluminescence experiments discussed above, despite their intrinsic lower density (~0.65 g cm^{-3}) compared to polystyrene (1.02 g cm^{-3}). Notably, the gas detection can be performed with an extremely high degree of reproducibility (±1.3% for 40 ns CW and 2.5 % for 400 ns, respectively), thus demonstrating the validity of the proposed experimental setup design and the quality of the synthesized porous nanoscintillators (Supplementary Material). On top of that, the PS microspheres emission is peaked at around 420 nm (Fig. S31), wherein the detection quantum efficiency (0.43) of the PMTs is significantly higher than that at 490 nm which corresponds to MOFs emission (0.25).[45] Therefore, a further improvement in gas detection efficiency can be envisaged by better matching the properties of the scintillators and detectors. Second, the expected increment using a longer coincidence window is less pronounced for Hf-DPA (ca.+25%) than for the microspheres (ca.+50%). This finding indicates that nanocrystals work better as fast scintillators with a negligible slow contribution, giving the detector a response that is closer to the ideal time-independent behaviour.

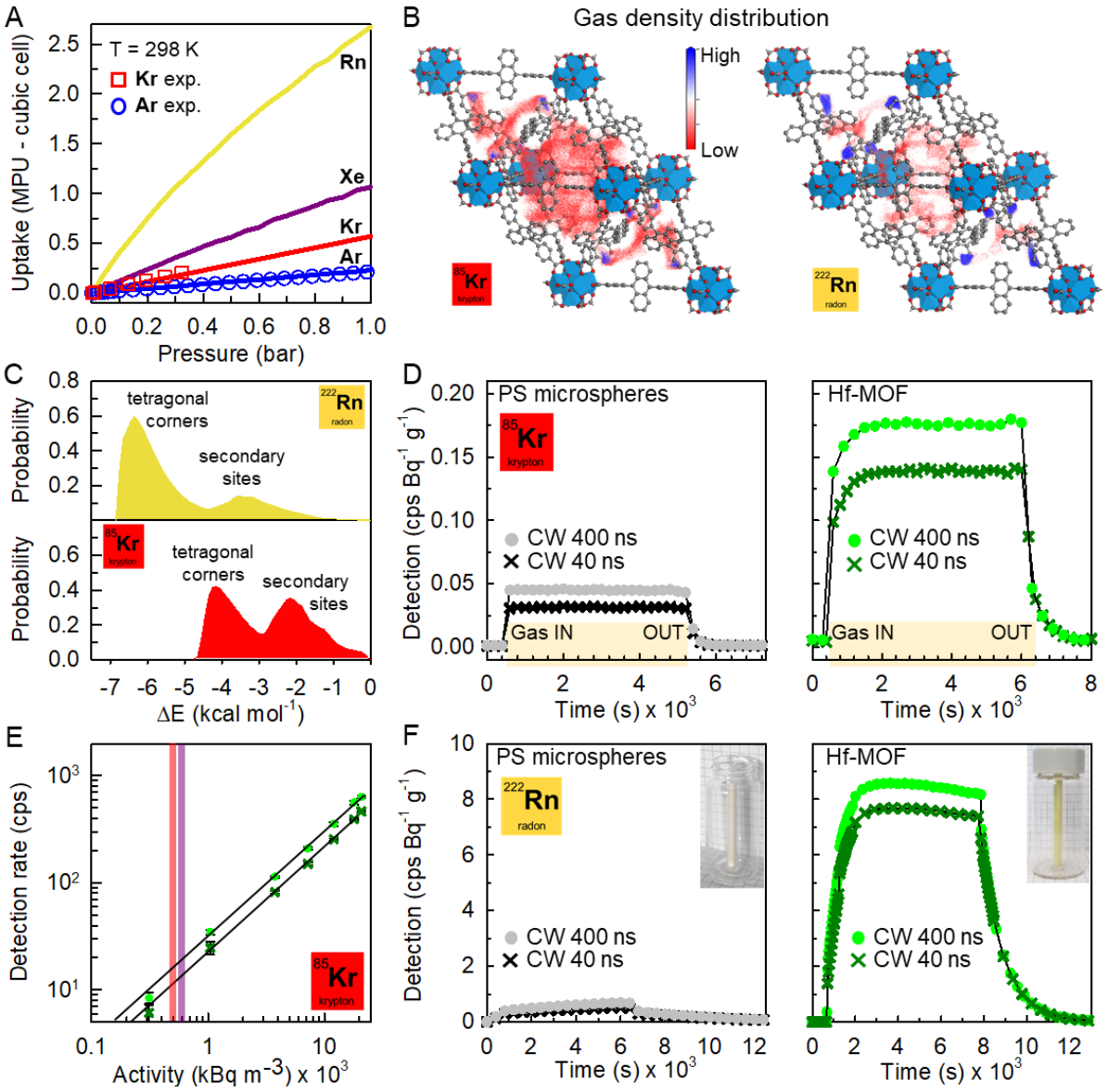

Figure 4 | Radioactive gas adsorption and detection by porous Hf-DPAs scintillating nanocrystals. (A) experimental Ar and Kr isotherms and Grand Canonical Montecarlo (GCMC) simulated adsorption isotherms of Ar, Kr, Xe and Rn for a cubic unit-cell of Hf-DPA (32.79×32.79×32.79 Å^3) at 298 K. The uptake is expressed in molecules per unit-cell (MPU). (B) Gas density distributions calculated at room temperature at constant pressure at 50 millibar by GCMC adsorption simulations for Kr, and Rn. Blue and red colours indicate the highest and lowest gas density in the pores. (C) Gas-matrix interaction energy distribution probability calculated at a constant pressure of 50 millibar and room temperature for Kr, Xe and Rn. (D) Double coincidence detection of ^{85}Kr by polystyrene (PS) microspheres powder and Hf-DPA nanocrystal powder using two different coincidence windows (CW) for detection (40 ns and 400 ns). The labels on the x-axis indicate when the radioactive gas has been injected into the detection device (Gas IN) and then washed out by a flux of clean air (Gas OUT). (E) Double coincidence detection rate of ^{85}Kr by the Hf-DPA powder as a function of the sample activity. The vertical lines mark the detection limit of a commercial device employed for detecting noble gas radionuclides (Refs. 46 and 47, red and violet line, respectively). (F) Double coincidence detection of ^{22}Rn by PS microsphere powder and Hf-DPA nanocrystal powder using different CW.

Third, the maximum recorded scintillation signal is reached with slower kinetics for the MOFs compared to the PS microspheres. Specifically, the rise time of the signal, calculated as time employed to reach 90% of the maximum plateau, is ~ 600 s for Hf-DPA nanocrystals vs. ~100 s for polystyrene microspheres. A similar effect is observed when removing the radionuclides from the sample chamber by purging it with clean air. The scintillation signal slowly switches off in 800 s for MOF nanocrystals, while it takes around half the time for the microspheres. These findings suggest that, in addition to the fast filling of interparticle space that also occurs within the packed microspheres, radionuclides are adsorbed within the MOF pores in agreement

with the experimental and simulated gas adsorption tests, thus promoting the interaction of the β radiation with the nanoscintillators which results in a better performance.

The versatility of our approach was further demonstrated by testing the performance of Hf-DPA nanocrystals as detectors with other radionuclides of interest, namely ^{222}Rn (with its four decay daughters at the equilibrium, which are α and high-energy β emitters, Fig.S40) and tritium ^{3}H. Considering the larger capture of Rn than Kr in the pores, the scintillating light output should be improved. Notably, as shown in Figure 4F, the detection efficiency is enhanced by twenty times with respect to PS microspheres, thus further supporting the validity of porous nanocrystals as scintillating detectors. Even for the elusive tritium, the nanocrystal powder shows a better sensitivity in detection counting rate, which is double that of the microspheres (Figure S41). This is a very important result since ^{3}H is one of the most difficult gas atoms to detect, given the relatively low energy of the β radiation emitted at a maximum energy of 18.6 keV with an average of 5.7 keV.[40]

Regarding Kr, we further tested the device detection ability as a function of the activity of the sample. This is a point of utmost importance since progressively more sensitive detectors are required. Figure 4E shows the result obtained by detecting ^{85}Kr at progressively lower concentrations in air. We successfully detected ^{85}Kr from an initial activity of 21 kBq·m^{-3} down to 0.3 kBq·m^{-3}, two orders of magnitude lower. Notably, the instrumental response is linear with the sample activity, thus suggesting the possibility of setting highly accurate calibrations of an operating device designed to detect ultralow activity levels. Even more importantly, we successfully detected an activity below the minimum value declared for commercial ^{85}Kr detectors (vertical lines) and in a device significantly smaller in size with an effective volume of detection as low as 0.5 cm^{-3}, owing to the porous scintillator's ability to adsorb the gases.[46,47] These remarkable results demonstrate that the prototype device presented here, although in its embryonal form, shows better sensitivity than that of the state-of-the-art devices and highlights the technological advantage of potentially using compact, easy-to-handle and cheaper devices. This work strongly supports the further development of radioactive gas detectors based on porous MOF nanocrystals as scintillators that can overcome current technological limitations.

CONCLUSIONS

In summary, we developed and fabricated specific scintillating MOF nanocrystals to detect radioactive noble gases. Their good luminescence and scintillation properties, combined with their characteristic porosity, allowed us to realize a prototype detector based on the prepared nanocrystals. An intensive study on a broad range of critical β-emitting radioactive gas was performed, namely the low energy β-emitter ^{3}H, the high energy β-emitter ^{85}Kr, and the β/α emitter ^{222}Rn. Remarkably, the prototype system used here showed improved performance compared to commercial powder-like materials currently tested for the realization of non-liquid detectors of these gases. Specifically, we found that ^{85}Kr can be detected with excellent sensitivity down to radioactivity values below the detection limit of commercial detectors. The obtained results are therefore stimulating not only from the scientific point of view, since radionuclide detection using porous scintillators has been demonstrated here for the first time, but also from the technological perspectives, hinting at a potential breakthrough by developing conceptually new optimized devices based on porous nanoscintillators. In this regard, it is worth pointing out that nanopowders cannot easily be used in the present form because of the practical problems of handling, especially from the perspective of an industrial production of detectors. Thus, we are working on the realization of a hierarchical porous architecture in which porous MOF nanoparticles are homogenously distributed in a porous polymeric host endowed with mesopores and macropores suitable for gas diffusion. In such a configuration, the highly stable MOF nanopowders will be employed to further concentrate and detect the radionuclides, thus realizing the first example of composite bulk porous scintillators for radioactive gas detection. The strongly improved handling of the material combined with the excellent detection properties of the porous MOF nanocrystals demonstrated here will provide a good step forward in the fabrication of high-tech ultrasensitive detectors, especially for low energetic radionuclides such the tritium produced in nuclear plants.

METHODS

Synthesis of Hf-DPA nanocrystals. Hf-DPA nanocrystals were synthesized using modulated solvothermal condition. Briefly, 9,10-bis(4-carboxyphenyl)anthracene (209.0 mg; 0.5 mmol) and $HfCl_4$ (160.0 mg; 0.5 mmol) were added to a 100 mL pyrex bottle with cleavable teflon-lined cap. Dry DMF (50 mL) and 400 µL of formic acid were added and the bottle was closed and sonicated for 60 seconds to obtain a well-dispersed mixture. The mixture was heated at 120 °C for 22 hours in a preheated oven. Then, the glass bottle was removed from the oven and cooled to RT. The yellowish solid was collected by filtration on a 0.2 µm PTFE membrane and washed with DMF (3 x 100 mL) and then $CHCl_3$ (3 x 100 mL). The powder was recovered and dried at 120 °C under high vacuum before further analysis. Yield: 178 mg (58 %) (See SI for further details on ligand and MOF preparation).

Hf-DPA analysis and characterizations. Powder X-ray diffraction (PXRD) patterns were collected on a Rigaku Smartlab using Cu-Kα radiation, while synchrotron radiation PXRD was performed at the ESRF ID22 beam line using a 0.354 Å wavelength. The crystal structure was refined by the Rietveld method combined with molecular mechanics and plane-wave density functional theory calculations (see Supplementary Information). The structure data are available at the Cambridge Crystallographic Data Centre repository, deposition number 2218565. The composition of Hf-DPA was studied by means of NMR spectroscopy in solution, solid-state NMR spectroscopy, Fourier-transform infrared spectroscopy, thermogravimetric analysis, scanning electron microscopy and EDS analysis. The gas sorption properties were investigated collecting N_2, Ar and Kr adsorption isotherms at 77 K up to saturation pressure and Ar and Kr at 298 K; hyperpolarized ^{129}Xe NMR experiments were performed by a home-built apparatus with a continuous-flow delivery of hyperpolarized Xe gas with a Bruker Avance 300 spectrometer operating at a Larmor Frequency of 83.02 MHz for ^{129}Xe (see Supplementary Information). The Xe and Rd adsorption isotherms at 298 K were carried out by Grand Canonical Montecarlo simulations.

Photoluminescence Studies. Absorption spectra were recorded using a Cary Lambda 900 spectrophotometer at normal incidence with Suprasil quartz cuvettes with a 0.1 cm optical path length and an integrating sphere to eliminate scattering effects. Steady-state PL spectra were acquired using a Varian Eclipse fluorimeter (bandwidth 1 nm) using quartz cuvettes of 0.1 cm optical path length. Time-resolved PL spectra of the nanocrystal dispersions were recorded by monitoring the emission decay of the samples at 435 nm. The nanocrystals were excited with a pulsed light-emitting diode at 340 nm (3.65 eV, pulse width 80 ps; EP-LED 340, Edinburgh Instruments). The MOF nanocomposites were excited with a pulsed laser at 405 nm (3.06 eV, pulse width 90 ps; EPL-405, Edinburgh Instruments) to avoid direct excitation of the host polymer matrix. PL decay times were measured at the maximum of the emission spectrum. Relative and absolute PL quantum yields were measured with different methods as described in the Supplementary Information. For experiments at cryogenic temperatures, the samples were excited by a frequency tripled pulsed Nd:YAG laser source at 3.49 eV (355 nm) operated at 10 kHz; the emitted light was collected using a custom apparatus featuring a liquid nitrogen-cooled, back-illuminated, and UV-enhanced charge-coupled device (CCD) detector (Jobin-Yvon Symphony II) coupled to a monochromator (Jobin-Yvon Triax 180) equipped with a 100 lines/mm grating.

Radioluminescence and scintillation studies. The samples were excited by unfiltered X-ray irradiation using a Philips PW2274 X-ray tube, with a tungsten target, equipped with a beryllium window and operated at 20 kV. At this operating voltage, X-rays are produced by the *Bremsstrahlung* mechanism due to the impact of electrons generated through a thermionic effect and accelerated onto the tungsten target. Cryogenic radioluminescence measurements are performed in the 10−320 K interval. Radioluminescence has been recorded on powder samples of 1 mm thickness in an aluminium sample holder. For comparison the radioluminescence spectra has been normalized by the mass of the investigated powder.

Scintillation has been recorded under pulsed X-rays with energies up to 25 keV generated with a repetition rate of 1 MHz by a picosecond diode laser at 405 nm (Delta diode from Horiba) focused on an X-ray tube (model N5084 from Hamamatsu). The resulting photons were collected by Kymera spectrograph (ANDOR) and detected by a hybrid PMT 140-C from Becker & Hickl GmbH. For decay-time measurements, the

photons were histogramed using a PicoHarp300 time-correlated single-photon counting (32 ps time/ bin) and for the time resolved spectra a MCS6A multiple-channel time analyzer was used (800 ps time/bin). Sub-nanosecond scintillation emission kinetics of the samples were measured with a Time Correlated Single Photon Counting (TCSPC) setup.

Thermally Stimulated Luminescence measurements. Wavelength-resolved TSL at cryogenic temperatures is carried out by using the same detection system as for RL measurements. Cryogenic TSL measurements are performed in the 10−320 K interval, with a linear heating rate of 0.1 K/s, after X-ray irradiation up to around 10 Gy. The dose values for X-ray irradiations were calibrated with an ionization chamber in air.

Radioactive gas detection experiments. The experiments are carried out using a unique gas bench developed at the CEA and allowing the production of radioactive gas atmospheres using very high activity standards. [48] Different sampling and dilution steps allow a precise control of the injected activity and a precise knowledge of the volumetric activity of each gas: at best, the relative standard uncertainty on the activity concentration are 0.4% for ^{222}Rn, 0.6% for ^{85}Kr, and 0.8% for ^{3}H (Supplementary Table 9). For each experiment, the same type of three step sequence is carried out. First, the measurement of the blank, by circulating clean air without additional radioactivity. Second, the measurement of scintillation by circulating the radioactive gas sample into the vial (4 mm diameter and 50 mm height, 0,1086 g for Hf-DPA and 0.3640 for PS microspheres, activity 10 kBq). Third, circulation of clean air into the device to remove the radioactive gas. The light photons produced by scintillation are measured using a metrological device developed to exploit the triple-to-double coincidence ratio (Supplementary Material, Fig. S39),[17] with a specific connection cap adapted to the radioactive gas flow in the scintillator.

ACKNOWLEDGMENTS

The authors acknowledge support from the European Community through the grant n° 899293, HORIZON 2020 – SPARTE. Financial support from the Italian Ministry of University (MUR) through grant PRIN 2020 – SHERPA n°H45F2100343000 and from Lombardy Region through “Enhancing photosynthesis” Award, n°. H45F21002830007. ESRF synchrotron facility in Grenoble (France) is thanked for access to the ID22 beamline (Project: HC-4781).

AUTHOR CONTRIBUTIONS

M.O., F.C., A.V. and A.M. conceived and performed the photoluminescence, radioluminescence experiments. J.P., C.X.B., S.P., C.Da., S.B. A.C. designed, synthesized and characterized the MOF nanocrystals. C.Du. managed the scintillation experiments. B.S., S. P. and P.M. designed, performed and analyzed the gas detection experiments. C.Du., B.S., A.C. and AM. conceived the project and wrote the paper. A.C. and AM. wrote the paper.

.

DECLARATION OF INTERESTS

The authors declare no competing interests.

REFERENCES

1 Bollhöfer, A. *et al.* Half a century of Krypton-85 activity concentration measured in air over Central Europe: Trends and relevance for dating young groundwater. *Journal of Environmental Radioactivity* **205-206**, 7-16 (2019).

2 Zeng, J. *et al.* Development of a well-type phoswich detector for low concentration Krypton-85 measurement. *Nuclear Instruments and Methods in Physics Research Section A: Accelerators, Spectrometers, Detectors and Associated Equipment* **1013**, 165634 (2021).

3 Huang, Y.-J. *et al.* Automated separation and analysis of krypton-85 from low-volume gaseous effluent of nuclear power plant. *Journal of Radioanalytical and Nuclear Chemistry* **323**, 213-222 (2020).

4 Aoyama, M. Long-term behavior of 137Cs and 3H activities from TEPCO Fukushima NPP1 accident in the coastal region off Fukushima, Japan. *Journal of Radioanalytical and Nuclear Chemistry* **316**, 1243-1252 (2018).

5 Cao, Y. *et al.* Long-term investigation of environmental radioactivity levels and public health around the Qinshan Nuclear Power Plant, China. *Scientific Reports* **12**, 4945 (2022).

6 Schoeppner, M. & Glaser, A. Present and future potential of krypton-85 for the detection of clandestine reprocessing plants for treaty verification. *Journal of Environmental Radioactivity* **162-163**, 300-309 (2016).

7 Ćujić, M. *et al.* Radon-222: environmental behavior and impact to (human and non-human) biota. *International Journal of Biometeorology* **65**, 69-83 (2021).

8 Abd Elkader, M. M., Shinonaga, T. & Sherif, M. M. Radiological hazard assessments of radionuclides in building materials, soils and sands from the Gaza Strip and the north of Sinai Peninsula. *Scientific Reports* **11**, 23251 (2021).

9 Rudin, C. M., Brambilla, E., Faivre-Finn, C. & Sage, J. Small-cell lung cancer. *Nature Reviews Disease Primers* **7**, 3 (2021).

10 Kissane, J., Neutze, J. A. & Singh, H. *Radiology fundamentals: Introduction to imaging & technology*. (Springer Nature, 2020).

11 Camfferman, F. A. *et al.* Diagnostic and predictive value of Doppler ultrasound for evaluation of the brain circulation in preterm infants: a systematic review. *Pediatric Research* **87**, 50-58 (2020).

12 Nichols, A. L. Status of the decay data for medical radionuclides: existing and potential diagnostic γ emitters, diagnostic β+ emitters and therapeutic radioisotopes. **110**, 609-644 (2022).

13 CTBTO. Comprehensive Nuclear-Test-Ban Treaty Organization. (2022).

14 European Union EURATOM Directive 59/2013 "Basic Safety Standards". (2013).

15 Aprile, E., Bolotnikov, A. E., Bolozdynya, A. I. & Doke, T. *Noble gas detectors*. (John Wiley & Sons, 2006).

16 Li, X. *et al.* Simultaneous determination of gross alpha/beta activities in water by liquid scintillation counting and its applications in the environmental monitoring. *Scientific Reports* **12**, 8281 (2022).

17 Sabot, B., Dutsov, C., Cassette, P. & Mitev, K. Performance of portable TDCR systems developed at LNE-LNHB. *Nuclear Instruments and Methods in Physics Research Section A: Accelerators, Spectrometers, Detectors and Associated Equipment* **1034**, 166721 (2022).

18 Kitagawa, S., Kitaura, R. & Noro, S. i. Functional porous coordination polymers. *Angewandte Chemie International Edition* **43**, 2334-2375 (2004).

19 Férey, G. Hybrid porous solids: past, present, future. *Chemical Society Reviews* **37**, 191-214 (2008).

20 Mezenov, Y. A., Krasilin, A. A., Dzyuba, V. P., Nominé, A. & Milichko, V. A. Metal–organic frameworks in modern physics: Highlights and perspectives. *Advanced Science* **6**, 1900506 (2019).

21 Lustig, W. P. *et al.* Metal–organic frameworks: functional luminescent and photonic materials for sensing applications. *Chemical Society Reviews* **46**, 3242-3285 (2017).

22 Doty, F., Bauer, C., Skulan, A., Grant, P. & Allendorf, M. Scintillating Metal-Organic Frameworks: A New Class of Radiation Detection Materials. *Advanced Materials* **21**, 95-101 (2009).

23 Perego, J. *et al.* Composite fast scintillators based on high-Z fluorescent metal–organic framework nanocrystals. *Nature Photonics* **15**, 393-400 (2021).

24 Perego, J. *et al.* Highly luminescent scintillating hetero-ligand MOF nanocrystals with engineered Stokes shift for photonic applications. *Nature Communications* **13**, 3504 (2022).

25 Yang, G. L., Jiang, X. L., Xu, H. & Zhao, B. Applications of MOFs as luminescent sensors for environmental pollutants. *Small* **17**, 2005327 (2021).

26 Jin, K., Lee, B. & Park, J. Metal-organic frameworks as a versatile platform for radionuclide management. *Coordination Chemistry Reviews* **427**, 213473 (2021).
27 Elsaidi, S. K. *et al.* Radiation-resistant metal-organic framework enables efficient separation of krypton fission gas from spent nuclear fuel. *Nature Communications* **11**, 3103 (2020).
28 Sozzani, P. *et al.* Nanoporosity of an organo-clay shown by hyperpolarized xenon and 2D NMR spectroscopy. *Chemical Communications*, 1921-1923 (2006).
29 Comotti, A., Bracco, S., Valsesia, P., Ferretti, L. & Sozzani, P. 2D multinuclear NMR, hyperpolarized xenon and gas storage in organosilica nanochannels with crystalline order in the walls. *Journal of the American Chemical Society* **129**, 8566-8576 (2007).
30 Bassanetti, I. *et al.* Flexible porous molecular materials responsive to CO 2, CH 4 and Xe stimuli. *Journal of Materials Chemistry A* **6**, 14231-14239 (2018).
31 Comotti, A. *et al.* Fluorinated porous organic frameworks for improved CO 2 and CH 4 capture. *Chemical Communications* **55**, 8999-9002 (2019).
32 Jameson, C. J. & de Dios, A. C. Xe nuclear magnetic resonance line shapes in nanochannels. *The Journal of chemical physics* **116**, 3805-3821 (2002).
33 Monguzzi, A. *et al.* Highly Fluorescent Metal–Organic-Framework Nanocomposites for Photonic Applications. *Nano Letters* **18**, 528-534, doi:10.1021/acs.nanolett.7b04536 (2018).
34 Ding, T. X., Olshansky, J. H., Leone, S. R. & Alivisatos, A. P. Efficiency of Hole Transfer from Photoexcited Quantum Dots to Covalently Linked Molecular Species. *Journal of the American Chemical Society* **137**, 2021-2029 (2015).
35 Korzhik, M., Tamulaitis, G. & Vasil'ev, A. N. *Physics of fast processes in scintillators*. Vol. 262 (Springer, 2020).
36 SW, S. M. (Cambridge University Press, Cambridge, 1985).
37 Vedda, A. *et al.* Trap-center recombination processes by rare earth activators in $YAlO_3$ single crystal host. *Physical Review B* **80**, 045113 (2009).
38 Liu, S. *et al.* Towards Bright and Fast Lu3Al5O12:Ce,Mg Optical Ceramics Scintillators. *Advanced Optical Materials* **4**, 731-739 (2016).
39 Cova, F., Moretti, F., Dujardin, C., Chiodini, N. & Vedda, A. Trapping Mechanisms and Delayed Recombination Processes in Scintillating Ce-Doped Sol–Gel Silica Fibers. *The Journal of Physical Chemistry C* **125**, 11489-11498 (2021).
40 Bé, M.-M. *et al.* Table of Radionuclides (vol. 3–A= 3 to 244). **5** (2006).
41 Dutsov, C., Cassette, P., Mitev, K. & Sabot, B. In quest of the optimal coincidence resolving time in TDCR LSC. *Nuclear Instruments and Methods in Physics Research Section A: Accelerators, Spectrometers, Detectors and Associated Equipment* **987**, 164846 (2021).
42 Dutsov, C., Cassette, P., Sabot, B. & Mitev, K. Evaluation of the accidental coincidence counting rates in TDCR counting. *Nuclear Instruments and Methods in Physics Research Section A: Accelerators, Spectrometers, Detectors and Associated Equipment* **977**, 164292 (2020).
43 Dutsov, C., Sabot, B., Cassette, P. & Mitev, K. Significance of the corrections for accidental coincidences in liquid scintillation counting measurements. *Journal of Radioanalytical and Nuclear Chemistry* **331**, 3303-3311 (2022).
44 Santiago, L. M., Bagán, H., Tarancón, A. & Garcia, J. F. Synthesis of plastic scintillation microspheres: Evaluation of scintillators. *Nuclear Instruments and Methods in Physics Research Section A: Accelerators, Spectrometers, Detectors and Associated Equipment* **698**, 106-116 (2013).
45 Hamamtsu Photonics R7600U PMT (2022).
46 Thermo Scientific™, T. FHT 59 E Noble Gas Monitor (2022).
47 MIRION TECHNOLOGIES Premium Analyse (2022)
48 Sabot, B., Rodrigues, M. & Pierre, S. Experimental facility for the production of reference atmosphere of radioactive gases (Rn, Xe, Kr, and H isotopes). *Applied Radiation and Isotopes* **155**, 108934 (2020).